# Spatial transcriptomic analysis of HIV and tuberculosis coinfection in a humanized mouse model reveals specific transcription patterns, immune responses and early morphological alteration signaling

Sitaramaraju Adduri[1#], Jose Alejandro Bohorquez[1#], Omoyeni Adejare[1], Diego Rincon[2], Torry Tucker[1], Nagarjun V Konduru[1], Guohua Yi[1*]

1. Department of Cellular and Molecular Biology, School of Medicine, The University of Texas Health Science Center at Tyler, 11937 US HWY 271, Tyler, TX 75708, USA
2. Unaffiliated pathologist

*Corresponding author: Guohua.yi@uttyler.edu

#Authors contributed equally to this work

**Abstract**

*Mycobacterium tuberculosis* (*Mtb*) and human immunodeficiency virus (HIV) coinfection is one of the biggest public health concerns worldwide. Both pathogens are adept at modulating immune response and, in the case of *Mtb*, even inducing structural modification of the affected tissue. The present study aimed at understanding the early phenotypical and functional changes in immune cell infiltration in the affected organ, using a humanized mouse model. The humanized mice were infected with either HIV or *Mtb* in single infection, or with both pathogens in coinfection. Three weeks after the infection, lung samples were collected, and spatial transcriptomics analysis was performed. This analysis revealed high infiltration of $CD4^+$ T cells in *Mtb* infection, but not in HIV or coinfection. Coinfected mice also showed a minimal number of NK cells compared to the other groups. In addition to infection status, histological features also influenced the immune cell infiltration pattern in the lungs. Two distinct airway regions with distinct immune cell abundance patterns were detected by spatial transcriptome profiling. A lymphoid cell aggregate detected in coinfection lung exhibited distinct transcript profile. The cellular architecture in the lymphoid cell aggregate did not follow the spatial patterns seen in mature granulomas. However, lymphoid cell aggregates exhibited granuloma gene expression signatures, and pathways associated with reactive oxygen species production, oxidative phosphorylation, and TGFβ and interferon signaling similar to granulomas. This study revealed specific transcription patterns, immune responses and morphological alteration signaling in the early stage of HIV and *Mtb* infections.

32 **Introduction**

33 Tuberculosis (TB), caused by *Mycobacterium tuberculosis* (*Mtb*), continues to be a major
34 public health concern. It has been estimated that as much as 25% of the world population is infected
35 with *Mtb*, although most of these cases will develop the latent form of TB (LTBI)[1]. One of the
36 main features of *Mtb* is its ability to modulate immune response to generate the latent disease form.
37 This immune modulation takes place in circulating immune cells, but also extends to tissue resident
38 cells, where *Mtb* is able to induce structural modification of the hosts tissue to create specialized
39 histological structures called granulomas[2,3]. These structures are composed of a necrotic core,
40 surrounded by different immune cell populations that contain the pathogen, preventing its spread
41 throughout the host and the development of active TB. Consequently, increasing interest has been
42 granted to the cellular infiltration in lung tissue during *Mtb* infection, in general, and in
43 granulomas, in particular[4-6]. The modification of cellular subsets in the affected organ and the inter-
44 cellular communication taking place provides an explanation for how they favor or deter pathogen
45 dissemination. It has been posed that there are multiple microenvironments present within
46 granuloma structures that induce an immunoregulatory environment with differential signaling, as
47 determined by pathway activation and cytokine production, playing a crucial role in the
48 maintenance of the structure[7].

49 Accordingly, local or generalized immune alterations can lead to changes in the granuloma
50 structures that can facilitate bacterial growth[8,9]. The Human immunodeficiency virus (HIV) is one
51 of the most important disruptors of the immune response and causes instability in the granuloma
52 structures[9]. Coinfection with HIV in *Mtb*-infected individuals severely increases the probability of
53 developing active TB[10], due to the generalized immunosuppression caused by the depletion of
54 CD4+ T cells, the main target for HIV infection, as well as the specific depletion of this cell subset

55 in the granulomas. Reports show that $CD4^+$ populations within granulomas are particularly
56 susceptible to HIV infection, due to increased expression of the CCR5 coreceptor[8]. Additionally,
57 given the importance of $CD4^+$ cells for $CD8^+$ cell maturation, HIV-induced $CD4^+$ cell depletion
58 reduces the circulating effector and memory $CD8^+$ cells and promotes immunosenescence in these
59 cells, rendering them dysfunctional[11].

60 Studies dedicated to understanding the cellular composition and intercellular networks
61 present locally in lung during *Mtb* infection and HIV/*Mtb* coinfection have focused on infection
62 models or samples in which the infections and structural changes are already set in the host, leaving
63 a gap in the knowledge of the early events taking place after infection[5-8,12]. This is partially due to
64 the use of stored human samples or non-human primate (NHP) animal models for these
65 experiments, which, though highly reliable, limit the availability of samples from early infection
66 timepoints. Recent reports show the feasibility of humanized mice as a model for the study of *Mtb*
67 and HIV[13,14]. These models are able to reproduce immune changes caused by infection, including
68 formation of lung granulomas. Given this, the aim of the present study was to evaluate the changes
69 in the cellular repertoire in the lung induced by HIV and *Mtb* in single infections, as well as in
70 coinfection, at an early timepoint in which granulomas have not been fully established.
71 Furthermore, we analyzed the transcriptomic changes in these cells, using a spatial approach, to
72 determine alterations in cytokine production in the affected areas. This allowed us to assess the
73 molecular processes taking place during infection, including evidence of changes in early
74 granuloma formation.

75 **Materials and methods**

76 **Generation of humanized mice**

77 Mice from the NOD.Cg-Prkdcscid Il2rgtm1Wjl Tg(CMV-IL3,CSF2,KITLG)1Eav
78 Tg(IL15)1Sz/J (NSG-SGM3-IL15) strain (The Jackson laboratory, Bar Harbor, ME), maintained
79 at the animal housing facility in the University of Texas Health Science Center at Tyler (UTHSCT)
80 were used for this study. Four to five weeks old mice were irradiated at a dose of 100cgy/mouse
81 for myeloablation. This was followed 6 hours later by intravenous (IV) inoculation with $2\times10^5$
82 human $CD34^+$ hematopoietic stem cells (STEMCELL technologies, Vancouver, Canada) per
83 mouse for humanization.

84 At 16 weeks after inoculation with human $CD34^+$ cells, humanization was confirmed in
85 accordance with a previously stablished protocol. Briefly, the whole blood samples were collected
86 by puncture of the submandibular vein and density gradient was used to separate peripheral blood
87 mononuclear cells (PBMCs). Once PBMCs were obtained, flow cytometry for specific human and
88 mouse immune cell markers was performed and humanization was confirmed for 13 mice. The
89 criteria for humanization included a positive human/mouse leukocyte ratio, as determined by
90 human $CD45^+$ vs. mouse $CD45^+$ expression, as well as the presence of multiple human immune
91 cell subsets, determined by markers for T-cells ($CD3^+$), B-cells ($CD20^+$), monocytes ($CD14^+$) and
92 natural killer (NK) cells ($CD56^+$), in accordance with a previously stablished protocol in our lab[13].

93 **Animal infection and experimental design**

94 Once mouse humanization was confirmed, the animals were randomly divided into 4
95 experimental groups (Figure 1A): A) No infection (n=3), B) HIV single infection (n=3), C) *Mtb*
96 single infection (n=3) and D) HIV/*Mtb* coinfection (n=4). Animals in groups C and D were infected
97 with aerosolized *Mtb*, H37Rv strain, using a Madison chamber[13,15]. Three non-humanized mice
98 were included in the infection chamber to confirm the infection dose. These three mice were
99 euthanized the following day and lung samples were collected, macerated and plated in 7H10

100 plates, supplemented with OADC (BD biosciences, Franklin Lakes, NJ). These mice confirmed
101 that the infection was successful, and the dose was determined to be ~40 CFU/lung.

102 Two days after the *Mtb* infection was carried out, mice in groups B and D were injected
103 intraperitoneally (IP) with $10^7$ TCID of HIV-1 BaL strain (obtained from NIH AIDS Reagent
104 Program). Two weeks after inoculation, whole blood sample was obtained and RNA was extracted
105 from plasma sample of these mice, using the NucleoSpin RNA isolation kit (Macherey-Nagel,
106 Allentown, PA), according to manufacturer's instructions. The viral RNA load in each animal was
107 determined by RT-qPCR, using a control standard (obtained from NIH AIDS Reagent Program)
108 with known quantities of HIV-1 genome copies, as previously described[16]. All HIV-inoculated
109 mice were positive for HIV RT-qPCR and showed similar viral RNA loads.

110 Three weeks after infection, all animals were humanely euthanized, in accordance with the
111 NIH guidelines for euthanasia of rodents using carbon dioxide, followed by confirmation by neck
112 dislocation. During necropsy, lung samples from each mouse were collected in accordance with
113 previous protocols. Briefly, once euthanasia was confirmed, the thoracic cavity was opened, and
114 the lungs were perfused and inflated by injection of 10% neutral buffered formalin (Thermo
115 Scientific, Waltham, MA) into the right heart ventricle and trachea, respectively. Afterwards,
116 samples were immediately submerged in the same buffer and kept at 4 °C until paraffin
117 embedding[17,18]. All animal procedures were approved by the UTHSCT Institutional Animal Care
118 and Use Committee (IACUC) (Protocol #763).

119 **10x Visium spatial transcriptome assay:**

120 Formalin fixed and paraffin embedded tissue sections were used to prepare sample slides
121 as per the 10x Genomics protocol (CG000518 and CG000520). RNA was isolated from the FFPE

122 sections using RNeasy FFPE kit (Qiagen, # 73504) following the kit protocol. Samples with
123 DV200 value of > 30% were selected for the spatial transcriptomics assay. The qualified samples
124 after H&E staining and image were decrosslinked based the protocol (CG000520) and the
125 sequencing libraries were prepared as per the manufacturer's protocol (CG000495). The quality of
126 the final libraries was examined using Agilent High Sensitive DNA Kit (#5067-4626) using
127 Agilent Bioanalyzer 2100 (Agilent Technologies, Santa Clara, USA). The qualified libraries were
128 sequenced using the paired-end sequencing on an Illumina Novaseq System (Illumina, Inc., USA).

129 **Visium spatial sequencing data analysis:**

130 With demultiplexed sequence fastq files and CytAssist tissue image as input, Space ranger
131 was used to map the reads to the latest human genome (hg38) and quantified read counts per spot.
132 The counts were normalized using 'sctranform' method in Seurat package[19]. For comparison
133 between different samples, the data was further normalized using minimum median counts
134 function. The samples were clustered and projected on UMAP. Find markers function was used
135 for identifying cluster specific markers and differentially expressed genes. Genes exhibiting a
136 minimum |log2FC| value of 2 at p.adj value of <0.05 were considered differentially expressed
137 genes. Pathway analysis was performed using GprofileR[20]. Loupe browser was used to examine
138 the spot-wise expression level of individual genes. Deconvolution of spatial gene expression
139 profiles were performed using RCTD package[21]. Single cell RNA sequencing (GSE192483) of
140 lung tissues with 18F-FDG avidity and nearby uninvolved tissues from six tuberculosis patients[22]
141 were used as reference for deconvolution analysis. Azimuth[23] was used for annotating the cells in
142 the reference dataset. Visualizations were created using ggplot2 package in R environment (4.1.1).

143 **Results**

144 **Immune cell infiltration patterns in the lungs are different for each infection type:**

145 We first investigated the effect of HIV and *Mtb* coinfection on immune responses in the
146 lung. In our earlier study on humanized mice model of coinfection, we observed that the $CD4^+$ T
147 cells depletion occurred rapidly after day 15 post infection and plateaued after day 28. Therefore,
148 to investigate the status of immune responses during rapid declining of $CD4^+$ cells, we euthanized
149 mice 21 days post infection and performed spatial transcriptome analysis of lung specimens from
150 humanized mice with HIV infection, *Mtb* infection and coinfection using 10x Genomics Visium
151 platform. The "No infection" group was used as control (Figure 1A). Excluding the poor-quality
152 regions and empty spots, our spatial transcriptomics analysis detected expression of 18,000 genes
153 across 3633, 2698, 2778, and 1397 spots in no infection, HIV, *Mtb*, and coinfection lungs,
154 respectively.

155 Since TB is predominantly a lung infectious disease, we assume that examining the
156 frequency of infiltration of different immune cells into lung will help us understand the immune
157 response against the pathogen. $CD4^+$ cells play crucial role in mitigating *Mtb* infection by releasing
158 signals that stimulate B cells to produce antibodies, cytotoxic T cells to kill infected cells, and
159 macrophages to engulf and destroy pathogen. Therefore, we were also interested in understanding
160 the effect of declining $CD4^+$ T cells titer on immune cell infiltration in lung tissues during
161 coinfection. To compare the abundance of immune cell markers across all 4 infections groups, we
162 normalized the spatial gene expression data from all samples using sctranform method followed
163 by recorrecting the SCT counts minimum median counts. This data is suitable for comparing the
164 gene expression between samples. As shown in Figure 1B, we observed that expression of CD4 is
165 minimal in HIV single infection and in coinfection compared to control and *Mtb* single infection.
166 This is expected as HIV infection and coinfection depletes $CD4^+$ T cell population. These results

167 suggest the possibility of existence of infection specific immune cell infiltration landscape in the
168 lungs.

169 To further investigate infiltration frequencies of immune cells into lungs across different
170 infection groups and control, we performed RCTD based cell type deconvolution analysis by
171 integrating the previously published single cell RNA sequencing data of human lung granuloma
172 (as detected by PET-CT) and their matched normal tissues of TB patients with our spatial
173 transcriptome data of all 4 infection groups. We first annotated the cell type labels of all cells in
174 scRNAseq data using Azimuth annotation database at the finest annotation level and transferred
175 these labels to our spatial transcriptome data during deconvolution analysis in 'full mode'. Since
176 Visium spots may span up to 6 individual cells, we opted to run deconvolution in 'full mode' as it
177 allows identification of any number of cells existing in each pixel. Corroborating with CD4 gene
178 expression in the tissues, cell type weights for $CD4^+$ T cells also showed the highest abundance of
179 $CD4^+$ T cells in *Mtb* infection while showing less abundance in HIV and coinfection mice (Figure
180 1C). Supporting previous reports, $CD4^+$ cells were less coinfection mice compared to HIV single
181 infection[24] (Figure 1C). Surprisingly, the abundance of nonclassical monocytes reduced in all
182 infections compared to control (Figure 1C). NK cells abundance was less in the coinfection mice
183 compared to the rest of the three groups. NK cell abundance was the highest in *Mtb* single infection
184 lung (Figure 1C). The lower levels of NK cell infiltration in coinfection compared to *Mtb* single
185 infection were observed in an earlier study[24]. The distribution of cell type weights of myeloid
186 lineage cells such as alveolar macrophages, $CCL3^+$ alveolar macrophages, classical monocytes,
187 monocyte derived macrophages, interstitial macrophages was similar across all groups suggesting
188 that infection status has minimal or no effect in the infiltration of these cells (Figure S1).

189 Altogether, these results suggest that lung tissue infiltration of various immune cell types depend
190 on the type of infection.

191 **Lung immune cell infiltration patterns differ based on infection status as well as local**
192 **histological milieu**

193 To understand the distinct patterns of immune cell infiltration into lungs, we performed
194 clustering of Visium spots across all 4 infection states together using Uniform Manifold
195 Approximation and Projection (UMAP) based on 50 principal components at a resolution of 0.9.
196 We observed a total of 14 clusters across 4 samples with no infection (12), HIV (11), *Mtb* (12),
197 and coinfection (12) (Figure 2A, S2A). Clusters 0-11 were present in all 4 samples while cluster
198 12 was detected neither in HIV nor in coinfection. Interestingly, cluster 13 was detected
199 exclusively in the coinfection group (Figure 3, S2A).

200 Interestingly, UMAP projection (Figure 2A) revealed a broad separation of all 14 clusters
201 into 3 distinct groups. These three cluster groups are represented by all four infection groups
202 (Figure 2A). Majority of the clusters, including clusters 0-3, 5-8, 10, 11 and 13 (total 11 clusters)
203 were placed together on the right on UMAP projection as a single large group (Figure 2B). These
204 spots correspond to alveolar/interstitial compartment of the lung across all 4 infection categories
205 (Figure 2B, S2B). Therefore, we aggregated these 11 clusters into one large cluster namely
206 'alveolar/interstitial' cluster for further analysis. Clusters 4 and 12 were placed separately together
207 and far from alveolar/interstitial cluster on UMAP projection (Figure 2C; represented in green and
208 blue, respectively). These spots belong to areas spanning airways in all four lungs (Figure S2C;
209 represented in green and blue, respectively). Therefore, we combined clusters 4 and 12 into one
210 cluster called 'airway_1' (Figure S2C; represented in red). Similarly, cluster 9, another distinct
211 cluster far away from the rest on the UMAP projection also harbored spots representing airways

212 across all four groups. It was also renamed as 'airway_2' for further analysis. Although, both
213 airway-1 and airway_2 clusters represent airways, they were not combined because they appeared
214 distinct from each other on UMAP projection. Interestingly, clusters were separated based on tissue
215 location and histological features rather than infection status. Altogether, these results suggest that
216 immune infiltration is strongly influenced by histological features compared to infection status in
217 our study.

218 To investigate the immune infiltration pattern differences between different clusters
219 associated with different histological location, we used the cell type weights obtained in
220 deconvolution analysis described in Figure 1. Abundance of $CD4^+$ T cells varied marginally
221 between alveolar/interstitial, airway_1, and airway_2 clusters with alveolar/interstitial and
222 airway_2 clusters exhibiting high abundance compared to airway_1 (Figure S2D). In contrast, the
223 abundance of monocyte derived macrophages was high in airway-1 compared to the rest (Figure
224 S2D). Interestingly, airway-2 cluster is enriched with $CCL3^+$ alveolar macrophages which are
225 known to be effective in phagocytosis of bacteria and other antigens (Figure 2D)[25] whereas
226 alveolar macrophages without high expression of CCL3 were marginally more abundant in
227 airway_1 cluster (Figure 2D). In contrast, airway_2 cluster and alveolar/interstitium clusters
228 exhibited a lower abundance of nonclassical monocytes compared to the airway_1 (Figure 2D).

229 Alveolar/interstium cluster is enriched with $CD8^+$ T cells and classical monocytes while
230 type 2 dendritic cells were less (Figure 2D). B cell, mast cells and type 1 dendritic cells did not
231 show any difference in abundance among the three clusters (Figure S2E). Altogether, these results
232 suggest that different histological regions may harbor district immune cell types. However, it is
233 not clear whether this differential abundance contributes to different immune responses.

234 **Cellular organization and composition of lymphoid cell aggregates markedly different from**
235 **typical mature tuberculosis granuloma**

236 Several previous studies investigated the cellular architecture of mature tuberculosis
237 granuloma. Granuloma may appear as a tiny lymphoid cell aggregate at initial stages and will
238 progress into a non-necrotic or central necrotic mature granuloma. Our understanding of the
239 cellular architecture of lymphoid cell aggregates is limited compared to mature granuloma.
240 Examination of hematoxylin (H&E) staining revealed the presence of a lymphoid aggregate in the
241 region of tissue subjected to spatial transcriptome profiling from coinfection mice. Focusing
242 exclusively on this region, we investigated 1) whether the cellular architecture of lymphoid
243 aggregate is similar or different from the mature granuloma, and 2) whether the lymphoid
244 aggregates show any transcriptomic changes characteristic of mature granuloma.

245 Surprisingly, we noticed that spots belonging to cluster 13, the only cluster on UMAP that
246 was exclusively detected in coinfection, spanned the entirety of the lymphoid cell aggregate in this
247 sample, suggesting that this lymphoid aggregate exhibit distinct transcription program compared
248 to the rest of the tissues across all 4 infection groups (Fig 3A). This lymphoid aggregate is present
249 in the interstitial region adjacent to a large airway and appears to have densely populated infiltrated
250 lymphoid cells on H& E staining (Fig 3B). On UMAP projection, cluster 13 is located together
251 within all clusters spanning interstitial region yet appears distinct from the rest of all interstitial
252 clusters (Figure 3C).

253 Necrotic granulomas are structured around a central core of necrotic cell debris in which
254 much of the bacteria are concentrated. The layers adjacent to necrotic core are mainly composed
255 of macrophages[2]. Layers of epithelioid macrophages surround the necrotic core interspersed with
256 other macrophage populations such as classical alveolar macrophages, monocyte derive

257 macrophages, lipid laden foamy macrophages, and giant cell[2]. A diversity of other immune cell
258 types is seen at the periphery as well as within the epithelioid layers of the granuloma. Non-
259 necrotic granulomas have similar structural arrangement except that they do not have necrotic
260 core[2]. However, cellular architecture and dynamics of these lymphoid aggregates are poorly
261 understood.

262 To decipher the cell type abundances in the Visium spots spanning the lymphoid cell
263 aggregate, we extracted cell type frequency predictions obtained from RCTD deconvolution
264 analysis. We labeled spots spanning the lymphoid cell aggregate as inner/core region, edge and
265 periphery, beginning from the center to the outer region (Figure 3D). To compare the abundance
266 of different immune cells predicted based on deconvolution analysis, we plotted a heatmap with
267 hierarchical clustering gene wise and spot wise (Figure 3E). Interestingly, we observed that the
268 spot wise clustering as shown by the column dendrogram separated peripheral spots from the inner
269 and edge spots accurately suggesting that cell distribution in these compartments is stratified based
270 on the location. In mature granuloma, B cells are present in the periphery while being absent or
271 minimal in the core. In contrast, we observed that in lymphoid aggregate, inner/core region spot is
272 highly abundant in B cells (Figure 3E). High abundance of B cells in the core region of the
273 lymphoid aggregate was also confirmed by the highest abundance of the mature B cell markers
274 like CD19 (Figure 3F), CD20 (MS4A1) (Figure S3A), and IgM (IGHM) (Figure S3B).
275 Plasmacytoid DCs are also highly enriched in the core and edge regions as shown in the heatmap
276 (Figure 3E), and corroborating with expression of plasmacytoid markers such as CD123 (IL3RA)
277 (Figure 3G), and CD303 (CLEC4C) (Figure S3C). Similarly, lymphoid aggregate harbors
278 nonclassical monocytes abundantly (Figure 3E). Nonclassical monocytes express high levels of
279 CD97 (ADGRE5), P2RX1, and Siglec10[26]. As expected, we observed a high abundance of CD97

280 (ADGRE5) (Figure S3D), P2RX1 (Figure S3E), and Siglec10 (Figure S3F) in the core or edge of
281 the lymphoid aggregate while their abundance being less in the periphery. We also observed
282 enrichment of plasma cells, DC2, CD4 T cells and nonclassical monocytes in the core of the lesion
283 (Figure 3E). In contrast, we observed NK cells, mast cells, macrophages, CD8 T cells, DC1 cells,
284 and classical monocytes on the periphery (Figure 3E).

285 Altogether, these results suggest that lymphoid cell aggregates may not essentially
286 originate with macrophage cells predominantly at the core. We speculate that granuloma
287 architecture may evolve into macrophage laden core and lymphocyte abundant periphery overtime.

288 **Lymphoid cell aggregates exhibited gene expression changes characteristic of granulomas**

289 Given that lymphoid cell aggregates did not show cellular architecture akin to granuloma,
290 we checked whether this lesion exhibits any transcriptomic changes seen in mature granulomas.
291 We examined the expression of genes that are part of gene sets related to granuloma in Molecular
292 Signatures Database (MSigDB). We analyzed the HP_GRANULOMA gene set consisting of
293 ACP5, CYBB, CYBC1, DNASE2, DOCK2, IRF8, NF1, and PIK3CG. Aggregated expression of
294 these genes was higher in the lymphoid aggregate region (Figure 4A) compared to the rest of the
295 lung tissue while individual genes also exhibited relatively high expression in the lymphoid
296 aggregate region (Figure S4). Similarly, another gene set named HP_ GRANULOMATOSIS
297 consisting of ASAH1, CTLA4, CYBA, CYBB, HLA-DPA1, HLA-DPB1, NCF1, NCF2, PRTN3,
298 and PTPN22 also exhibited higher expression in lymphoid aggregate compared to rest of the tissue
299 (Figure 4A, S5A). These results suggest that gene expression changes characteristic of mature
300 granulomas appear to emerge early into the development of the granuloma from lymphoid
301 aggregate.

302 Encouraged by these results, to understand the molecular changes occurring early stages
303 of the granuloma development, we performed pathway analysis to identify signaling pathways
304 enriched in the lymphoid cell aggregate region. We performed differential expression analysis
305 using Seurat 'find-markers' function to identify genes that were up or downregulated in cluster 13.
306 At a log2FC cut off 2 and p.adj value of 0.05, we detected 383 upregulated and 20 downregulated
307 genes. Pathway analysis was performed independently for both up and down-regulated genes.
308 Multiple pathway terms representing immune response to viral, *Mtb*, and bacterial infections, B
309 cell and NK cell activity, cytokine signaling, glucose metabolism and oxidative phosphorylation,
310 ROS generation, interferon signaling and activation of several Interferon regulatory factor
311 transcriptional factors were significantly enriched in genes upregulated in the lymphoid cell
312 aggregate (Figure 4B, Supplementary Table 1). Interestingly, oxidative phosphorylation and ROS
313 generation are crucial for pathogen killing inside granulomas[27]. Transcriptional targets of several
314 interferon regulatory factors (IRF5, IRF7, and IRF9) were enriched in upregulated genes (Figure
315 4B-C, Supplementary Table 1). Type I-interferon signaling is known to promote *Mtb* infection by
316 facilitating the release of neutrophil extracellular traps[28] and suppressing interferon gamma and
317 interleukin 1α/β signaling[29].

318 Intriguingly, similar analysis on downregulated genes revealed enrichment of multiple
319 pathways related to downregulation of inhibitory SMAD expression in lymphoid cell aggregate
320 suggesting that this lesion may harbor activated TGFβ signaling (Figure 4D, Supplementary Table
321 2). This was corroborated by decreased expression of SMAD6 which inhibits TGFβ signaling and
322 upregulation of TGFβ signaling ligands namely TGFβ1/2 in the same tissue region, suggesting that
323 TGFβ signaling is activated (Figure 4E). Altogether, these results suggest that lymphoid cell

324 aggregates may show several characteristics of granulomas even before they evolve into mature
325 granulomas.

326 **Discussion**

327 Novel spatial transcriptomic technologies provide a powerful tool to assess molecular and
328 immunological changes in situ in various tissues, thus understanding the effects of infection on the
329 host and allowing for in-depth knowledge of how disease is developed or avoided[30,31]. In the
330 present study, these technologies were used to evaluate the early changes caused by HIV and *Mtb*
331 infections and coinfection in humanized mouse lung tissues. Although lung is the main target organ
332 for *Mtb*, it's also greatly affected by the generalized immunosuppression caused by HIV[9] due to
333 massive depletion of $CD4^+$ T cell population[8,9]. The increase in $CD4^+$ T cells after *Mtb* single
334 infection relates to increased migration to the affected sites to control the pathogens[4]. Meanwhile,
335 the severe local depletion of this CD4+ T cell subset in HIV-infected hu-mice (with or without *Mtb*
336 coinfection) is a staple of HIV that has been previously described[8] and found in the present work.
337 The approach used in the present study allowed for the detection of alterations in less studied
338 populations, mainly non-classical monocytes and NK cells. Interestingly, even though HIV and
339 *Mtb* single infection increased the NK cell population, when compared to the uninfected control,
340 coinfection had the opposite effect. A similar pattern was reported for certain phenotypes of NK
341 cells in HIV/*Mtb* coinfected patients and it is likely that alterations in this cell subset vary in
342 accordance with the phenotypes differentiated in the subject[32].

343 A considerable portion of the differences evidenced in cell populations presented in the
344 tissue corresponded not only with infection, but rather with different histological regions, with
345 areas including bronchi and major airways being clearly differentiated from interstitial tissue.
346 However, even within the clustered airway regions, viral and bacterial infection modified the

347 phenotypical landscape. This is shown by the high presence of alveolar macrophages expressing
348 CCL3 in the airway regions from all the infected animals, in contrast with the uninfected controls.
349 CCL3 is known to aid in the activation of alveolar macrophages and efforts to control bacterial
350 and viral pathogens[25,33]. Recently, it was also found to be increased in COVID-19 patients suffering
351 alveolar damage, supporting the important role of these cells for pulmonary immunity[34].

352 The finding of a structurally organized and clearly differentiated cell cluster with a unique
353 transcriptomic profile, in the sample from HIV/*Mtb* coinfected mouse, provides insight into the
354 early phenotypical and signaling changes induced by this type of infection. Spatial analysis showed
355 the presence of both lymphoid and myeloid cells in the lymphoid aggregates. Remarkably, despite
356 being infected with HIV and showing generalized $CD4^+$ T cell depletion in the tissue, this cell
357 subset was found within the structure, mainly in the inner part and accompanied by B cells and
358 plasmacytoid DCs. It should be noted that the manner in which the cell subsets are organized in
359 the lymphoid structure found in the HIV/*Mtb* coinfected sample is not compatible with that found
360 in mature granulomas, which generally have a necrotic core, surrounded by macrophages and
361 epithelioid cells with lymphocytes in the outer layer[2,3,7]. Conversely, the unique structure found in
362 the HIV/*Mtb* coinfected hu-mouse tissue lacks evidence of necrosis and the monocytic cells within
363 it are in the outer layer. This is likely due to the fact that this cell aggregate is in the early stages
364 of forming a granulomatous structure and the time after infection has not yet been sufficient to
365 generate necrosis. This is in line with previous findings in murine *Mtb* model which detected the
366 presence of inflammatory cell aggregates, mainly adjacent to circulation or bronchi as early as 2
367 weeks after infection, with the first necrotic changes being detected around 1 month after
368 infection[35,36]. Moreover, our results show that the transcriptomic alterations found in this
369 premature granuloma-like structure are compatible with the signaling reported for mature

370 granulomas, supporting the idea that the lymphoid aggregate found in this sample is in the early
371 stages of granuloma formation.

372 The process of granuloma establishment involves precise modulation of the interferon
373 pathway, mainly through the upregulation of multiple IRFs, as shown in the cells present in this
374 granuloma-like structure. Some of the IRF genes found to be upregulated in the lymphoid
375 aggregate from the present study have been previously reported to be crucial for granuloma
376 formation and maintenance, as IRF8 deficient mice proved unable to form these structures and
377 limit *Mtb* growth after infection[37]. However, the increased transcription of different IRF genes
378 suggests regulation of the IFN response using multiple mechanisms, including cell differentiation
379 and innate immunity. This is likely a response to the initial induction of type-I IFNs and activation
380 of the IFN pathway and IFN stimulated genes (ISGs) after infection, but the relevance of this
381 multiple approach to IFN modulation in more advanced stages of structural remodeling remains to
382 be elucidated. Reports suggest that mature granulomas (after 9 weeks post infection) do not show
383 upregulation of these pathways, while others report increased IRF transcription in these structures,
384 though mainly in non-immune cell types (fibroblasts)[6,38].

385 Consequently, the activation of immune response by the IFN pathway leads to increased
386 energy requirements in the immune cells present in the lymphoid aggregate, as exemplified by the
387 upregulation of oxidative phosphorylation related genes. This has been established as an important
388 metabolic consequence of both HIV and *Mtb* infections, as well as HIV/*Mtb* coinfection[39-41]. Our
389 results show that the generalized metabolic changes induced by HIV/*Mtb* coinfection also occurs
390 locally in the affected tissues and, specifically in the affected areas, starting at an early stage of the
391 infection.

392 In addition, contrasting with the regulation of the IFN pathway, our results show a lack of
393 TGFβ regulation. TGFβ inhibition of *Mtb*-specific $CD4^+$ T cells has been found to play a role in
394 the maintenance of *Mtb* within mature granuloma structures in rhesus macaque and mice models[42].
395 This cytokine and its associated pathways has also been proposed as a determinant of myeloid cell
396 differentiation in TB granulomas[43], while virtual modeling results have suggested an enhancement
397 of bacterial clearance in absence of TGFβ[44].

398 **Conclusions**

399 The modulation of immune response by pathogens is an important determinant for the
400 outcome of infection. This can take the form of generalized immunosuppression, as caused by
401 HIV, or more nuanced modulation of immune response, as induced by *Mtb*. The results from the
402 present study show the effects of these pathogens, whether in single infection or coinfection, in
403 lung tissue of a humanized mouse model at an early timepoint after inoculation. Our findings
404 suggest that alterations in cellular infiltration and structural remodeling of the tissue begin to take
405 place early after infection and closely resemble those that have been previously reported for
406 humans and other animal models. This further validates the use of the NSG-SGM3-IL15 mouse
407 strain as a reliable animal model that can reproduce multiple aspects of HIV and *Mtb* infections,
408 as well as HIV/*Mtb* coinfection. Nevertheless, future studies, using higher resolution spatial
409 transcriptomics, will further elucidate the transcriptomic changes in lung immune cell populations
410 at a single cell level. This information will provide further detail into specific changes in different
411 cell populations, both in terms of phenotype and signaling and open up new avenues of research
412 to generate intervention strategies that improve infection outcome in patients infected with HIV
413 and *Mtb*.

414 **Conflict of interest:**

Authors declare no conflicts of interest.

**Acknowledgements:**

We thank the technical support from the Cancer Prevention and Research Institute of Texas (CPRIT RP240610). We thank the Texas Advanced Computing Center (TACC) at The University of Texas at Austin for providing computational resources that have contributed to the research results reported within this paper. We'd like to thank Joshua Kleam at the Histopathology core at UTHCT, for his help with this study and Drs. Buka Samten and Amy Tvinnereim for their aid in the animal experiment.

**Funding**

This work was supported by a NIH Common funds/National Institute of Allergy and Infectious Diseases grant UG3AI150550, a National Institute of Allergy and Infectious Diseases grant R01AI184551, and a National Heart, Lung, and Blood Institute grant R01HL125016 to GY

**References**

1 WHO. Global Tuberculosis Report. (WHO, Geneva, Switzerland, 2023).

2 Cronan, M. R. In the Thick of It: Formation of the Tuberculous Granuloma and Its Effects on Host and Therapeutic Responses. *Frontiers in Immunology* **13** (2022). https://doi.org:10.3389/fimmu.2022.820134

3 McCaffrey, E. F. *et al*. The immunoregulatory landscape of human tuberculosis granulomas. *Nat Immunol* **23**, 318-329 (2022). https://doi.org:10.1038/s41590-021-01121-x

4 Bromley, J. D. *et al*. CD4(+) T cells re-wire granuloma cellularity and regulatory networks to promote immunomodulation following Mtb reinfection. *Immunity* **57**, 2380-2398 e2386 (2024). https://doi.org:10.1016/j.immuni.2024.08.002

5 Carow, B. *et al*. Spatial and temporal localization of immune transcripts defines hallmarks and diversity in the tuberculosis granuloma. *Nat Commun* **10**, 1823 (2019). https://doi.org:10.1038/s41467-019-09816-4

6 Krausgruber, T. *et al*. Single-cell and spatial transcriptomics reveal aberrant lymphoid developmental programs driving granuloma formation. *Immunity* **56**, 289-306 e287 (2023). https://doi.org:10.1016/j.immuni.2023.01.014

7 Qiu, X. *et al.* Spatial transcriptomic sequencing reveals immune microenvironment features of Mycobacterium tuberculosis granulomas in lung and omentum. *Theranostics* **14**, 6185-6201 (2024). https://doi.org:10.7150/thno.99038

8 Foreman, T. W. *et al.* CD4 T cells are rapidly depleted from tuberculosis granulomas following acute SIV co-infection. *Cell Rep* **39**, 110896 (2022). https://doi.org:10.1016/j.celrep.2022.110896

9 Kaushal, D., Singh, D. K. & Mehra, S. Immune Responses in Lung Granulomas during Mtb/HIV Co-Infection: Implications for Pathogenesis and Therapy. *Pathogens* **12** (2023). https://doi.org:10.3390/pathogens12091120

10 Azevedo-Pereira, J. M. *et al.* HIV/Mtb Co-Infection: From the Amplification of Disease Pathogenesis to an "Emerging Syndemic". *Microorganisms 2023, Vol. 11, Page 853* **11** (2023-03-27). https://doi.org:10.3390/microorganisms11040853

11 Bohorquez, J. A., Jagannath, C., Xu, H., Wang, X. & Yi, G. T Cell Responses during Human Immunodeficiency Virus/Mycobacterium tuberculosis Coinfection. *Vaccines (Basel)* **12** (2024). https://doi.org:10.3390/vaccines12080901

12 Sawyer, A. J. *et al.* Spatial mapping reveals granuloma diversity and histopathological superstructure in human tuberculosis. *J Exp Med* **220** (2023). https://doi.org:10.1084/jem.20221392

13 Bohorquez, J. A. *et al.* A Novel Humanized Mouse Model for HIV and Tuberculosis Co-infection Studies. *bioRxiv*, 2024.2003.2005.583545 (2024). https://doi.org:10.1101/2024.03.05.583545

14 Lepard, M. *et al.* Comparing Current and Next-Generation Humanized Mouse Models for Advancing HIV and HIV/Mtb Co-Infection Studies. *Viruses* **14** (2022). https://doi.org:10.3390/v14091927

15 Feng, Y. *et al.* Exposure to Cigarette Smoke Inhibits the Pulmonary T-Cell Response to Influenza Virus andMycobacterium tuberculosis. *Infection and Immunity* **79**, 229-237 (2011). https://doi.org:10.1128/iai.00709-10

16 Butler, S. L., Hansen, M. S. T. & Bushman, F. D. A quantitative assay for HIV DNA integration in vivo. *Nature Medicine* **7**, 631-634 (2001). https://doi.org:10.1038/87979

17 Morton, J. & Snider, T. A. Guidelines for collection and processing of lungs from aged mice for histological studies. *Pathobiology of Aging & Age-related Diseases* **7**, 1313676 (2017). https://doi.org:10.1080/20010001.2017.1313676

18 Davenport, M. L., Sherrill, T. P., Blackwell, T. S. & Edmonds, M. D. Perfusion and Inflation of the Mouse Lung for Tumor Histology. *J Vis Exp* (2020). https://doi.org:10.3791/60605

19 Hao, Y. *et al.* Dictionary learning for integrative, multimodal and scalable single-cell analysis. *Nat Biotechnol* **42**, 293-304 (2024). https://doi.org:10.1038/s41587-023-01767-y

20 Kolberg, L., Raudvere, U., Kuzmin, I., Vilo, J. & Peterson, H. gprofiler2 -- an R package for gene list functional enrichment analysis and namespace conversion toolset g:Profiler. *F1000Res* **9** (2020). https://doi.org:10.12688/f1000research.24956.2

21 Cable, D. M. *et al.* Robust decomposition of cell type mixtures in spatial transcriptomics. *Nat Biotechnol* **40**, 517-526 (2022). https://doi.org:10.1038/s41587-021-00830-w

22 Wang, L. *et al*. Single-cell RNA-sequencing reveals heterogeneity and intercellular crosstalk in human tuberculosis lung. *J Infect* **87**, 373-384 (2023). https://doi.org:10.1016/j.jinf.2023.09.004

23 Hao, Y. *et al*. Integrated analysis of multimodal single-cell data. *Cell* **184**, 3573-3587 e3529 (2021). https://doi.org:10.1016/j.cell.2021.04.048

24 Xiao, G. *et al*. Uncovering the Bronchoalveolar Single-Cell Landscape of Patients With Pulmonary Tuberculosis With Human Immunodeficiency Virus Type 1 Coinfection. *J Infect Dis* **230**, e524-e535 (2024). https://doi.org:10.1093/infdis/jiae042

25 Lindell, D. M., Standiford, T. J., Mancuso, P., Leshen, Z. J. & Huffnagle, G. B. Macrophage inflammatory protein 1alpha/CCL3 is required for clearance of an acute Klebsiella pneumoniae pulmonary infection. *Infect Immun* **69**, 6364-6369 (2001). https://doi.org:10.1128/IAI.69.10.6364-6369.2001

26 Wong, K. L. *et al*. Gene expression profiling reveals the defining features of the classical, intermediate, and nonclassical human monocyte subsets. *Blood* **118**, e16-31 (2011). https://doi.org:10.1182/blood-2010-12-326355

27 Song, E. *et al*. Chronic granulomatous disease: a review of the infectious and inflammatory complications. *Clin Mol Allergy* **9**, 10 (2011). https://doi.org:10.1186/1476-7961-9-10

28 Chowdhury, C. S. *et al*. Type I IFN-mediated NET release promotes Mycobacterium tuberculosis replication and is associated with granuloma caseation. *Cell Host Microbe* **32**, 2092-2111 e2097 (2024). https://doi.org:10.1016/j.chom.2024.11.008

29 Donovan, M. L., Schultz, T. E., Duke, T. J. & Blumenthal, A. Type I Interferons in the Pathogenesis of Tuberculosis: Molecular Drivers and Immunological Consequences. *Front Immunol* **8**, 1633 (2017). https://doi.org:10.3389/fimmu.2017.01633

30 Marx, V. Method of the Year: spatially resolved transcriptomics. *Nat Methods* **18**, 9-14 (2021). https://doi.org:10.1038/s41592-020-01033-y

31 Williams, C. G., Lee, H. J., Asatsuma, T., Vento-Tormo, R. & Haque, A. An introduction to spatial transcriptomics for biomedical research. *Genome Med* **14**, 68 (2022). https://doi.org:10.1186/s13073-022-01075-1

32 Gao, J. *et al*. Mtb/HIV co-infection immune microenvironment subpopulations heterogeneity. *Int Immunopharmacol* **143**, 113341 (2024). https://doi.org:10.1016/j.intimp.2024.113341

33 Sadee, W. *et al*. Human alveolar macrophage response to Mycobacterium tuberculosis: immune characteristics underlying large inter-individual variability. *Res Sq* (2023). https://doi.org:10.21203/rs.3.rs-2986649/v1

34 Garcia-Prieto, C. A. *et al*. Spatial transcriptomics unveils the *in situ* cellular and molecular hallmarks of the lung in fatal COVID-19. *bioRxiv*, 2024.2007.2003.601404 (2024). https://doi.org:10.1101/2024.07.03.601404

35 Tsai, M. C. *et al*. Characterization of the tuberculous granuloma in murine and human lungs: cellular composition and relative tissue oxygen tension. *Cell Microbiol* **8**, 218-232 (2006). https://doi.org:10.1111/j.1462-5822.2005.00612.x

36 Driver, E. R. *et al*. Evaluation of a mouse model of necrotic granuloma formation using C3HeB/FeJ mice for testing of drugs against Mycobacterium tuberculosis. *Antimicrob Agents Chemother* **56**, 3181-3195 (2012). https://doi.org:10.1128/AAC.00217-12

37 Rocca, S. *et al*. Interferon regulatory factor 8-deficiency determines massive neutrophil recruitment but T cell defect in fast growing granulomas during tuberculosis. *PLoS One* **8**, e62751 (2013). https://doi.org:10.1371/journal.pone.0062751

38 Mehra, S. *et al*. Granuloma correlates of protection against tuberculosis and mechanisms of immune modulation by Mycobacterium tuberculosis. *J Infect Dis* **207**, 1115-1127 (2013). https://doi.org:10.1093/infdis/jis778

39 Herbert, C., Luies, L., Loots, D. T. & Williams, A. A. The metabolic consequences of HIV/TB co-infection. *BMC Infectious Diseases* **23** (2023). https://doi.org:10.1186/s12879-023-08505-4

40 Masson, J. J. R. *et al*. Assessment of metabolic and mitochondrial dynamics in CD4+ and CD8+ T cells in virologically suppressed HIV-positive individuals on combination antiretroviral therapy. *PLOS ONE* **12** (30 ago 2017). https://doi.org:10.1371/journal.pone.0183931

41 Singh, V. *et al*. Mycobacterium tuberculosis-Driven Targeted Recalibration of Macrophage Lipid Homeostasis Promotes the Foamy Phenotype. *Cell Host & Microbe* **12** (2012/11/15). https://doi.org:10.1016/j.chom.2012.09.012

42 Gern, B. H. *et al*. TGFβ restricts expansion, survival, and function of T cells within the tuberculous granuloma. *Cell Host & Microbe* **29**, 594-606.e596 (2021). https://doi.org:10.1016/j.chom.2021.02.005

43 Peters, J. M. *et al*. Systematic deconstruction of myeloid cell signaling in tuberculosis granulomas reveals IFN-γ, TGF-β, and time are associated with conserved myeloid diversity. *bioRxiv*, 2024.2005.2024.595747 (2024). https://doi.org:10.1101/2024.05.24.595747

44 Warsinske, H. C., Pienaar, E., Linderman, J. J., Mattila, J. T. & Kirschner, D. E. Deletion of TGF-beta1 Increases Bacterial Clearance by Cytotoxic T Cells in a Tuberculosis Granuloma Model. *Front Immunol* **8**, 1843 (2017). https://doi.org:10.3389/fimmu.2017.01843

562 **Figure legends**

563 **Figure 1. Cell type abundance variations between control, HIV, Mtb and coinfection mice as**
564 **predicted by cell specific marker analysis and cell type deconvolution analysis.**

565 A) The experimental protocol. The number of mice was four per group. B) Expression levels of
566 CD4 genes were shown across the four groups. D) Cell type weights for each spot in the samples
567 based on RCTD analysis were plotted for each infection types. X axis shows cell types weights
568 which are proportional to the cell type abundance in the tissue. Difference in cell weight
569 distributions was computed using Kruskal Wallis test followed by Dunn's test for pairwise
570 comparisons. P were adjusted for multiple hypothesis testing using Bonferroni correction method.
571 Significance levels are indicated as *P < .05, **P < .01, ***P < .001, and ****P < .0001. Figure
572 created using Biorender.com

573 **Figure 2. Identification clusters based on gene expression of all tissue spots from no infection,**
574 **HIV, Mtb, and coinfection mice lungs using Seurat package.**

575 A) Clusters from all four samples projected on UMAP and color based on cluster identifier (left)
576 and sample type (right). B) Alveolar/interstitium cluster (shown in blue), airway_1 (shown in
577 blue/green) and airway-2 (shown in red) clusters on UMAP projection. D) Cell type weights
578 obtained in RCTD deconvolution analysis were plotted for each cluster. Y axis shows cell types
579 weights which are proportional to the cell type abundance in the corresponding cluster. Color key
580 indicated the cluster identifier. Difference in cell weight distributions was computed using Kruskal
581 Wallis test followed by Dunn's test for pairwise comparisons. P values were adjusted for multiple
582 hypothesis testing using Bonferroni correction method. Significance levels are indicated as *$P$ <
583 .05, **$P$ < .01, ***$P$ < .001, and ****$P$ < .0001.

584 **Figure 3: Characterization of the unique cluster (cluster 13) detected in HIV/Mtb coinfection**
585 **mouse lung.**

586 A) Spatial mapping of cluster 13 which was detected exclusively in coinfection lung. Clusters were
587 identified on UMPA projection of all Visium spots passing quality control from all four infection
588 groups combined. Spots representing cluster 13 were highlighted in blue. B) Hematoxylin staining
589 of lung region matching with cluster 13 location in coinfection lung. This region contains a circular
590 lymphoid aggregate formed by dense lymphocyte infiltration located within the interstitial region
591 and close to two airways. C) UMAP projection of all Visium spots passing quality control from all
592 four infection groups highlighting the location of cluster 13. D) Projection of the Visium spots
593 overlapping with lymphoid aggregate shown in Figure 3B. The spots were labeled as core/inner
594 region, edge, and periphery depending on the location and were highlighted according to the label
595 with different colors. E) Heatmap showing the cell type abundances all the spots highlighted in
596 Figure 3D. Columns show individual spots spanning the lymphoid aggregate. The rows show the
597 immune cells detected in the spots. Color intensities represent the abundance of each cell in each
598 spot. Row and column dendrograms represent the similarity between cell abundances and
599 individual spots, respectively, as computed using hierarchical clustering. F) Spatial map of
600 expression of CD19, a mature B cell marker within and around the lymphoid aggregate. Spot-wise
601 gene expression data was projected on hematoxylin staining image of the lung tissue. Color key
602 represent the level of transcript expression. G) Expression of CD123 (IL3RA), plasmacytoid
603 markers in the same region as described for Figure 3F.

604 **Figure 4: gene expression changes and pathway analysis of lymphoid aggregate**

605 A) Aggregated gene expression of granuloma and granulomatosis gene sets from MSigDB
606 projected on hematoxylin stain of lungs from coinfection mice. Spot-wise gene expression

607 aggregate was projected on lymphoid cell aggregate and its surround tissue. Color key represents
608 aggregate of expression values of all the genes in the granuloma gene set (DOCK2, CYBC1,
609 PIK3CG, CYBB, IRF8, NF1, DNASE2, and ACP5) and granulomatosis gene set (DOCK2,
610 CYBC1, PIK3CG, CYBB, IRF8, NF1, DNASE2, and ACP5). B) Top 20 pathways based on p.adj
611 identified in over representation analysis on genes upregulated in cluster 13 spanning lymphoid
612 cell aggregate in coinfection mice. Gene ratios were computed with the percentage of total DEGs
613 in the given pathway term. C) Expression levels of interferon regulatory factors enriched among
614 upregulated genes in lymphoid cell aggregate were projected individually on lymphoid cell
615 aggregate and its surround tissue. D) Top 20 pathways identified in over representation analysis
616 on gene down regulated in cluster 13 as shown like figure 4B. E) Down regulation of SMAD6, an
617 inhibitory SMAD and upregulation of TGFB1/2 in lymphoid cell aggregate. Gene expression
618 levels quantified in spatial transcriptomics analysis were projected on hematoxylin-stained tissue
619 section. A, C, E) Color key represents aggregate/individual gene expression values in log2 scale.

620

621 **Figure 1:**

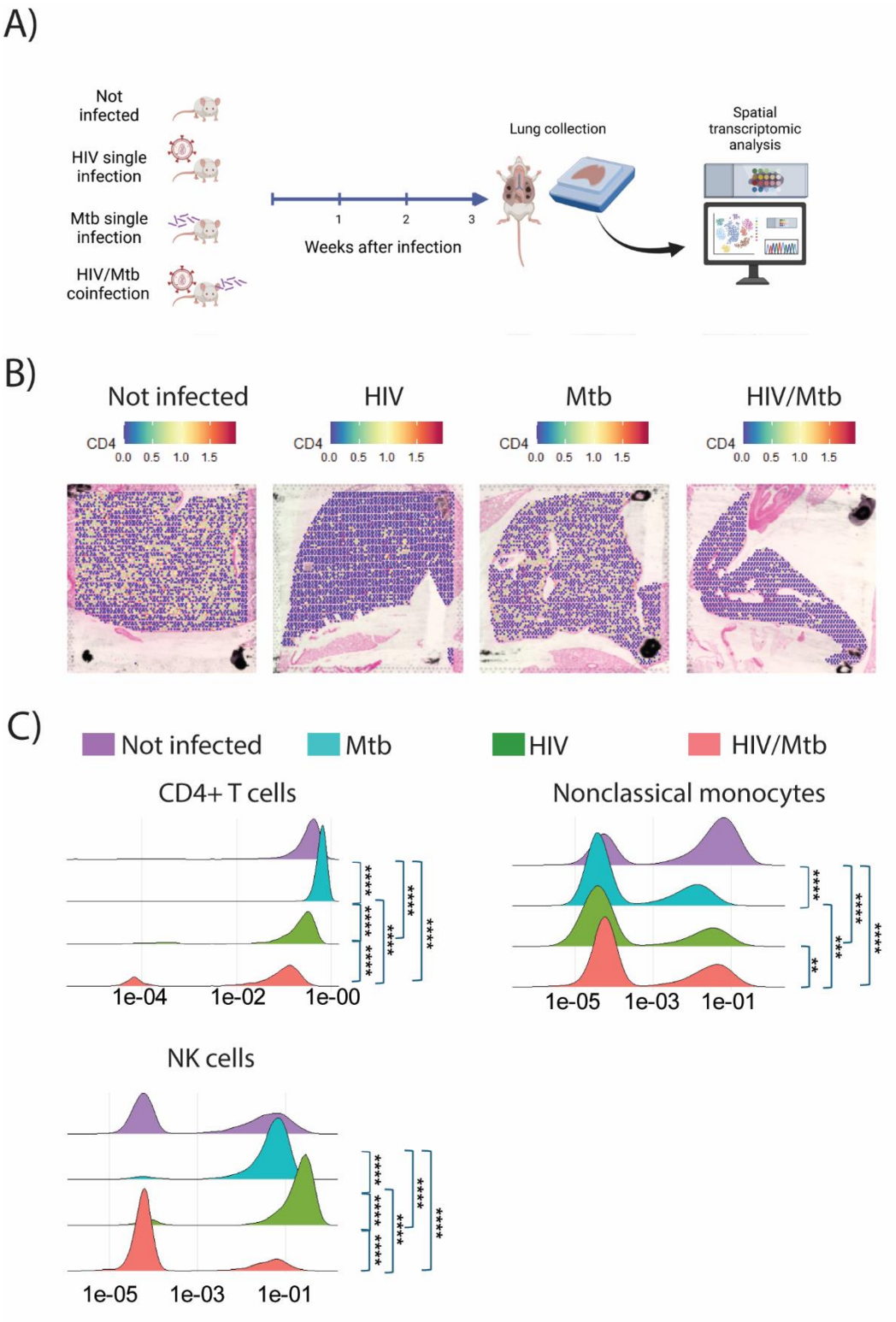


622

623 **Figure 2:**

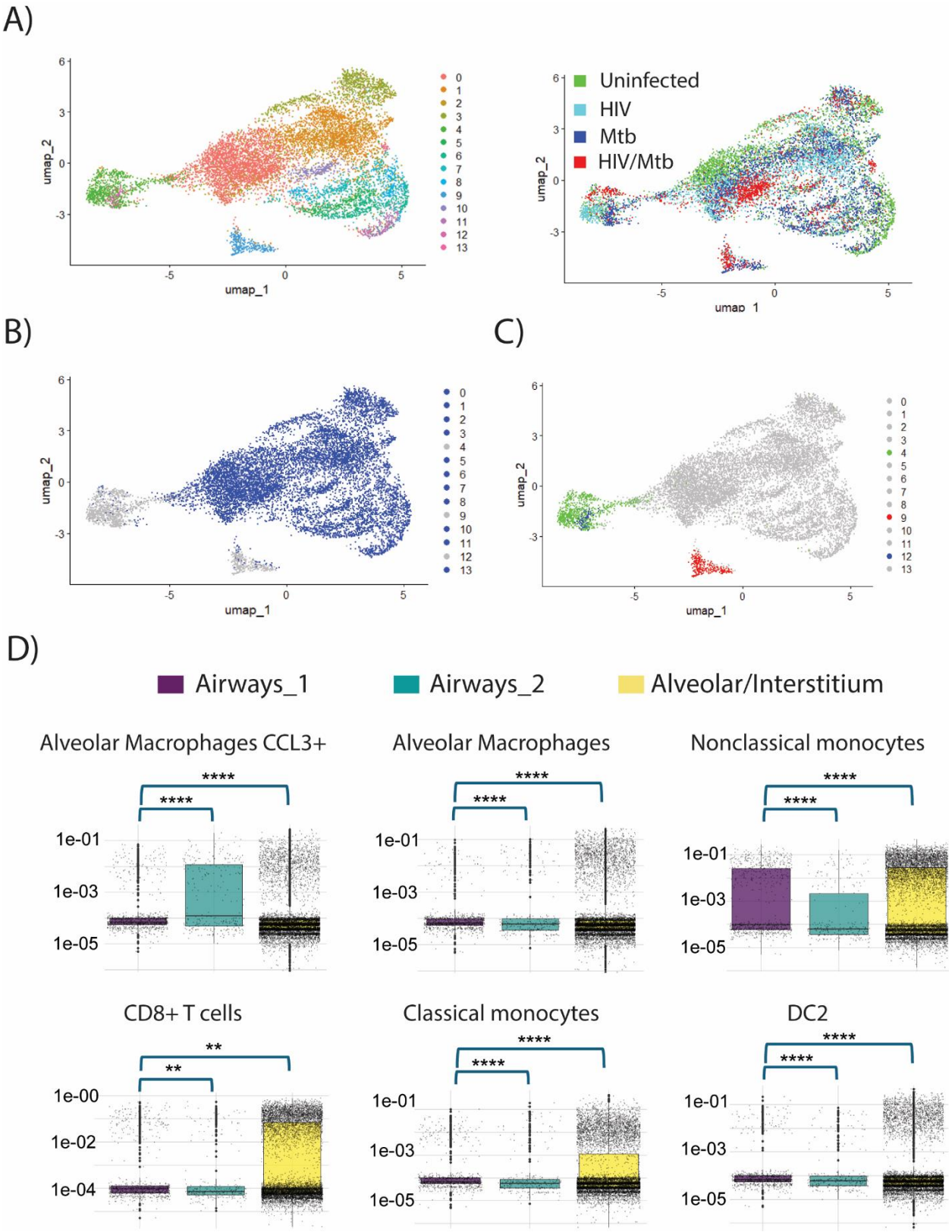


624

**Figure 3:**

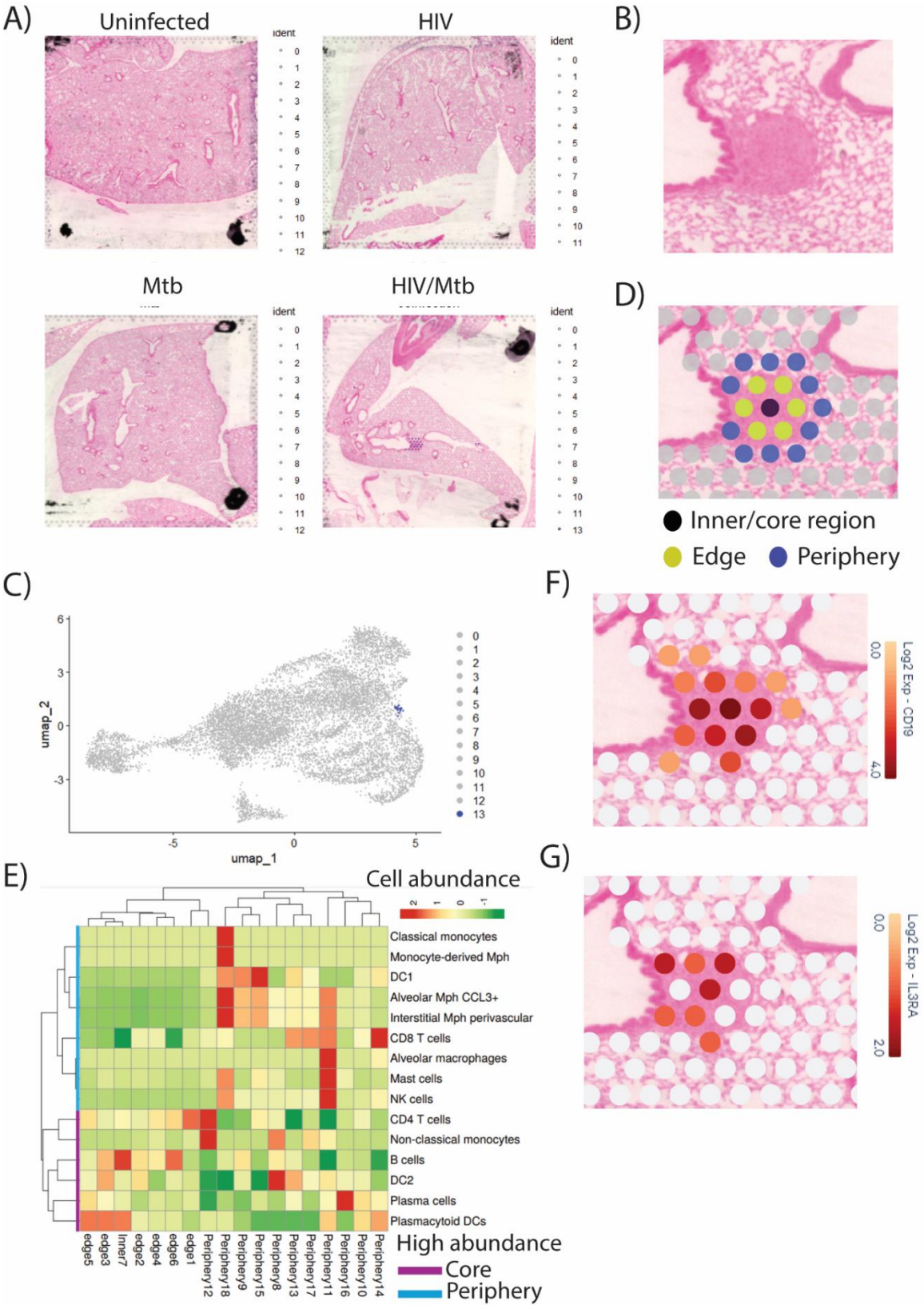
A)
Uninfected
HIV
Mtb
HIV/Mtb
ident
B)
D)
Inner/core region
Edge
Periphery
C)
umap_1
umap_2
F)
Log2 Exp - CD19
G)
Log2 Exp - IL3RA
E)
Cell abundance
Classical monocytes
Monocyte-derived Mph
DC1
Alveolar Mph CCL3+
Interstitial Mph perivascular
CD8 T cells
Alveolar macrophages
Mast cells
NK cells
CD4 T cells
Non-classical monocytes
B cells
DC2
Plasma cells
Plasmacytoid DCs
High abundance
Core
Periphery

**Figure 4:**

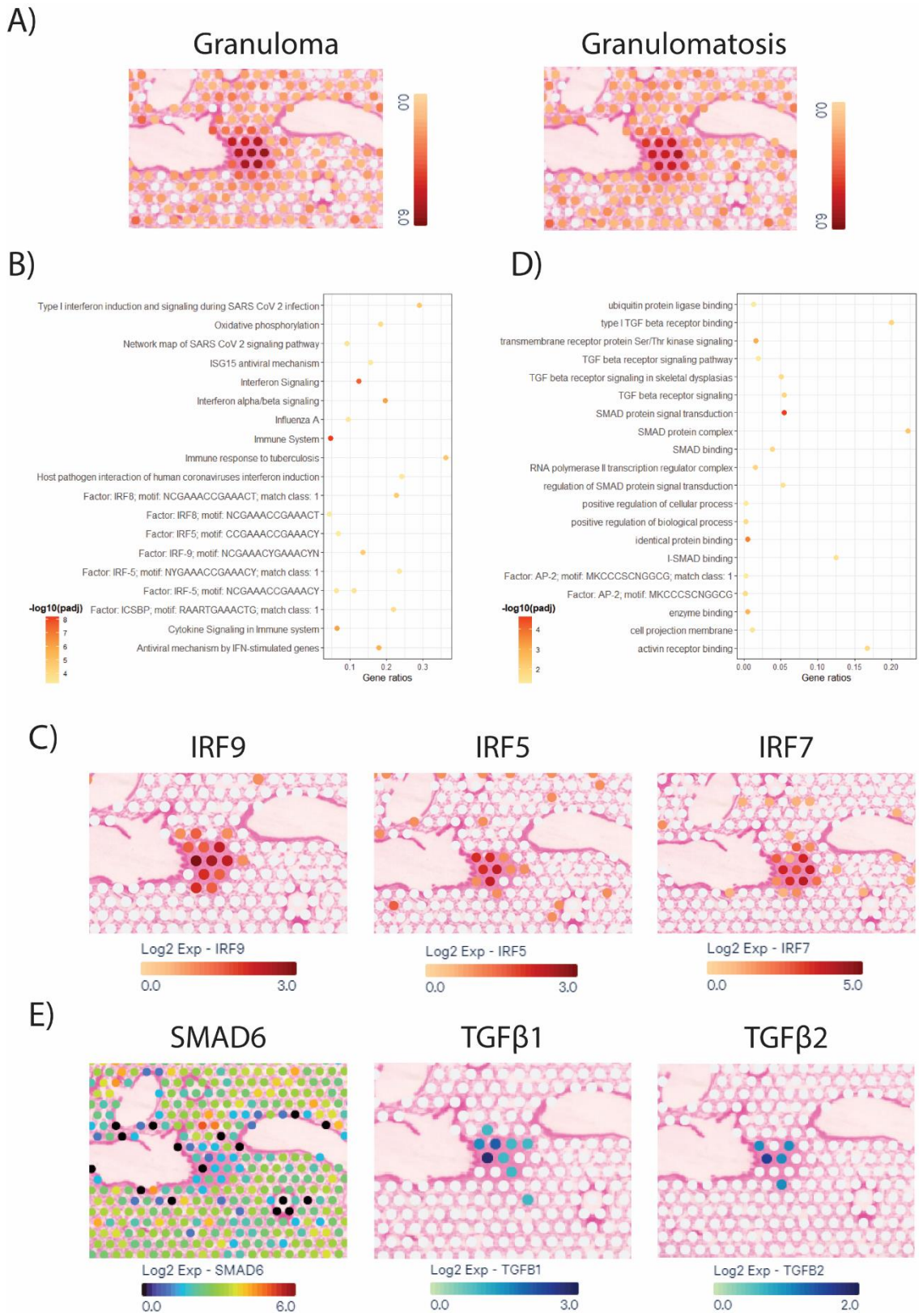
A)
Granuloma
Granulomatosis
B)
Type I interferon induction and signaling during SARS CoV 2 infection
Oxidative phosphorylation
Network map of SARS CoV 2 signaling pathway
ISG15 antiviral mechanism
Interferon Signaling
Interferon alpha/beta signaling
Influenza A
Immune System
Immune response to tuberculosis
Host pathogen interaction of human coronaviruses interferon induction
Factor: IRF8; motif: NCGAAACCGAAACT; match class: 1
Factor: IRF8; motif: NCGAAACCGAAACT
Factor: IRF5; motif: CCGAAACCGAAACY
Factor: IRF-9; motif: NCGAAACYGAAACYN
Factor: IRF-5; motif: NYGAAACCGAAACY; match class: 1
Factor: IRF-5; motif: NCGAAACCGAAACY
Factor: ICSBP; motif: RAARTGAAACTG; match class: 1
Cytokine Signaling in Immune system
Antiviral mechanism by IFN-stimulated genes
-log10(padj)
Gene ratios
D)
ubiquitin protein ligase binding
type I TGF beta receptor binding
transmembrane receptor protein Ser/Thr kinase signaling
TGF beta receptor signaling pathway
TGF beta receptor signaling in skeletal dysplasias
TGF beta receptor signaling
SMAD protein signal transduction
SMAD protein complex
SMAD binding
RNA polymerase II transcription regulator complex
regulation of SMAD protein signal transduction
positive regulation of cellular process
positive regulation of biological process
identical protein binding
I-SMAD binding
Factor: AP-2; motif: MKCCCSCNGGCG; match class: 1
Factor: AP-2; motif: MKCCCSCNGGCG
enzyme binding
cell projection membrane
activin receptor binding
-log10(padj)
Gene ratios
C)
IRF9
IRF5
IRF7
Log2 Exp - IRF9
0.0
3.0
Log2 Exp - IRF5
0.0
3.0
Log2 Exp - IRF7
0.0
5.0
E)
SMAD6
TGFβ1
TGFβ2
Log2 Exp - SMAD6
0.0
6.0
Log2 Exp - TGFB1
0.0
3.0
Log2 Exp - TGFB2
0.0
2.0